

Anomalous Response of Floating Offshore Wind Turbine to Wind and Waves I: Model & MCMC

Yihan Liu ^(1,2) and Michael (Misha) Chertkov ⁽¹⁾

⁽¹⁾ Program in Applied Mathematics & Department of Mathematics, University of Arizona, Tucson, AZ 85721, USA

⁽²⁾ Virginia Tech, Blacksburg, VA 24061, USA

Correspondence to chertkov@arizona.edu

December 5, 2024

Abstract

We study the Floating Offshore Wind Turbine (FOWT) dynamic response to high wind velocity scenarios utilizing an extensive Markov Chain Monte Carlo (MCMC) simulation involving 10,000 trials of a reduced model from [3] with a blade-pitch PID controller. The research emphasizes analysis of extreme events in surge, pitch and heave of FOWT, identifying and categorizing them based on their statistics, correlations and causal relations to wind and waves. A significant insight is the differentiation of anomalies into short-correlated and long-correlated types, with the latter primarily influenced by wind conditions. For example, one of our findings is that while specific wave conditions may amplify anomalies, wind remains the predominant factor in long-term anomalous pitch behaviors. We anticipate that further development of this analysis of the operation's critical extreme events will be pivotal for advancing control strategies and design considerations in FOWTs, accommodating the turbulent environment they encounter.

1 Introduction

The global emphasis on environmental protection has prompted an increased reliance on renewable energy sources. In the forefront, wind power become America's largest source of renewable energy avoiding 334 million metric tons of **CO₂** emissions in 2022 [2]. Recently, floating offshore wind turbines (FOWTs) have been deployed widely in deep water (greater than 60 m), showcasing a multitude of advantages over onshore and fixed-bottom offshore wind turbines. For instance, FOWTs operating in deep marine environments offer a higher wind intensity, thereby enhancing power production. They also omit visual and noise pollution to reduce cost, and reduce land use. The expansion deployment of FOWTs underscores the critical necessity for reliable, high-performance wind turbines. However, this structure operating in such environments is subjected to the relentless forces of stochastic wind and wave perturbations that can significantly impart mechanical stress on various turbine components. Hence, studying rare or extreme events for FOWTs is crucial for several reasons:

1. **Safety and Structural Integrity:** Rare events, such as extreme winds or high waves, can pose significant risks to the structural integrity of FOWTs. Understanding these events helps in designing platforms that can withstand such extremes, and optimizing operation strategies for existing designs, ensuring the safety of the structure.
2. **Reliability and Performance:** The reliability of offshore wind turbines is critical for ensuring a consistent and uninterrupted supply of renewable energy. By studying rare events, engineers can predict and mitigate potential failures or performance issues, leading to more reliable energy production and reduced downtime.
3. **Risk Management:** Understanding the risks associated with rare events is crucial for insurance purposes and risk management strategies. Detailed studies of these events enable more accurate risk

assessments, which in turn influence insurance premiums and the development of risk mitigation strategies.

For this study, we provide a preliminary analysis of the rare events of FOWTs subject to high wind speed. the NREL 5MW wind turbine, an established solution for offshore development was selected [4]. There are three popular design approaches for FOWT platform: the tensioned leg platform (TLP)-based FOWT, the spar-buoy FOWT, and the semi-submerged FOWT [6] (see Fig. 1). Each design variant, along with its corresponding reduced-order modeling approach is outlined in [?]. For our research, we have opted for the TLP-based FOWT due to its outstanding low root mean square accelerations and negligible heave and pitch motions [5]. Utilizing the simple reproducible Betti model can be used for control (original use in [3]) but is also generally useful when needing to work with many samples, uncertainty, and also looking for rare events as it has direct access to the rod tension, aerodynamic and hydrodynamic loads, and various forces acting on the system.

The operation of wind turbines contains four regions, each defined by distinct wind speeds. Regions 1 and 4 correspond to wind velocities that are below the cut-in threshold and beyond the cut-out threshold, which are typically not of interest. Wind turbines in Region 2 strive to maximize power production, usually by maintaining a fixed blade pitch angle and employing a generator torque controller. Wind turbines in Region 3 aim to regulate rotor speed. The generator torque controller keeps the generator power constant and uses a blade pitch angle controller to regulate the rotor speed. In this paper, we limit our simulations on FOWT response to high wind speeds corresponding to Region 3. This necessitates adjustments to the controller. As described in Section 2.5, this is achieved by an additional tuning process for the blade-pitch controller, building on the baseline controller provided by [4].

The structure of this paper is as follows: Section 2 provides a detailed description of the Betti Model, elaborating on the dynamics of the FOWT's platform and the drivetrain, alongside the modeling of wind and wave impacts and the implementation of the Blade-Pitch Controller. Section 3 delves into the Markov Chain Monte Carlo Simulation, presenting an overview of the simulation results and a thorough analysis of extreme events, including differentiating between short- and long-correlated anomalies. The paper concludes in Section 4 with a summary of findings and future research directions. Additionally, Appendices A, B, and C offer supplementary information on coordinate systems transition, weight contributions of tie rod lines, and an example TurbSim input, respectively, providing a comprehensive overview of the methodologies and considerations underlying our research.

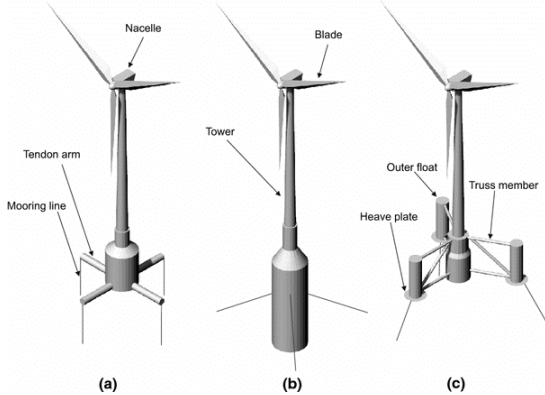


Figure 1: Three designs of FOWT. (a). TLP-based FOWT, (b). Spar-buoy FOWT, (c). Semi-submerged FOWT. Taken from [6].

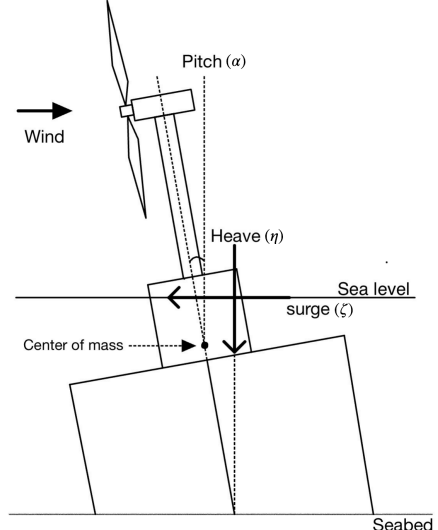


Figure 2: The 2-dimension representation of TLP-based FOWT in the Betti model.

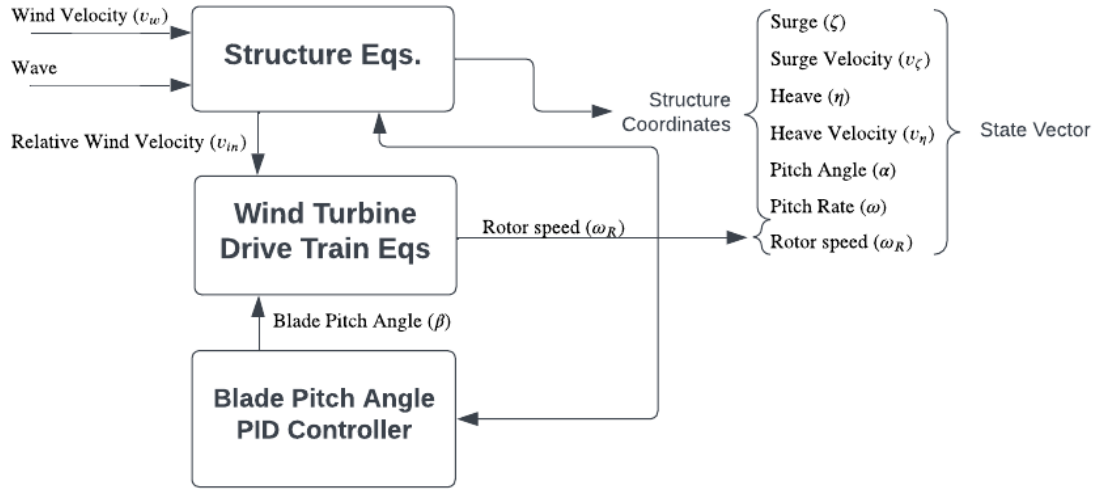


Figure 3: Scheme of the simulation flow of the Betti model.

2 Description of the Betti Model [3]

Our modeling approach for simulation of the FOWTs dynamics, adapted from Betti's model [3], is illustrated in Fig. 3. The model describes the dynamics of the 7-component state vector, where 6 components are associated with the platform of the FOWT, and one component is associated with the drivetrain (rotating) part. For completeness, we would also like to mention other open-source reduced-order models of wind turbines discussed in the literature, specifically QuLAF [?] and RAFT [?].

The mainfram FOWT within the Betti model accounts for a 2-dimensional perspective, resulting in 3 degrees of freedom (DOF): surge (ζ), heave (η), pitch (α), along with their respective velocities (v_ζ , v_η , ω) total of the six-states. It is described below in Section 2.1.

The drivetrain modeling of the FOWT rotating part describes dynamics of the angular frequency (rotor speed) of the turbine, ω_R , detailed in Section 2.2.

The choice of the coordinate system is significant for both the platform and drivetrain parts of the model. The model establishes a two-dimensional coordinate system with a horizontal axis at sea level, pointing opposite to the wind direction, and a vertical axis at the central anchor bolt pointing downward (Fig. 2). The position is measured at the center of gravity of the entire structure accounting for both the platform and the tower. This is in deviation from the coordinate system from [3] associated with the center of the platform only. All graphical representations in this paper adhere to the Right-Hand Cartesian Coordinate System RCCS [5] and align with the OpenFAST conventions. The method to transition between the two coordinate systems (utilized in this paper and in [3]) is described in Appendix A.

Another important aspect of the overall FOWT modeling we use is in its dependence on the exogenous wind and wave fluctuations, which is discussed in Section 2.3.

Finally, it is also imperative to close the introductory portion of the Section by mentioning the significance of the wind turbine controller, discussed in Section 2.5, on the modeling efforts overall.

2.1 Modeling Dynamics of the FOWT's Platform (non-rotating part)

The mechanical part of the Betti model is stated in terms of the three Degrees Of Freedom (DOF) – three “coordinates” – surge, heave, and pitch – and their “velocities” yields to six states satisfy Newton’s laws describing the balance of the respective inertial terms and forces (or torques):

$$\mathbf{E}\dot{\mathbf{x}} = \mathbf{F} \quad (1)$$

with the state vector

$$\mathbf{x} = [\zeta \ v_\zeta \ \eta \ v_\eta \ \alpha \ \omega]^T \quad (2)$$

the mass matrix

$$\mathbf{E} = \begin{bmatrix} 1 & 0 & 0 & 0 & 0 & 0 \\ 0 & M_X & 0 & 0 & 0 & M_d \cos(\alpha) \\ 0 & 0 & 1 & 0 & 0 & 0 \\ 0 & 0 & 0 & M_Y & 0 & M_d \sin(\alpha) \\ 0 & 0 & 0 & 0 & 1 & 0 \\ 0 & M_d \cos(\alpha) & 0 & M_d \sin(\alpha) & 0 & J_{TOT} \end{bmatrix} \quad (3)$$

and the force vector

$$\mathbf{F} = \begin{bmatrix} v_\zeta \\ Q_\zeta + M_d \omega^2 \sin(\alpha) \\ v_\eta \\ Q_\eta - M_d \omega^2 \cos(\alpha) \\ \omega \\ Q_\alpha \end{bmatrix}. \quad (4)$$

M_X , M_Y , M_d are the mass parameters and J_{TOT} is the inertial parameter.

The Q -components of the \mathbf{F} array get contributions from the following terms (We present respective expressions here without explanations, which can be found in [3].):

Weight Forces: (5)

$$Q_\zeta^{(we)} = 0, \quad Q_\zeta^{(we)} = (M_n + M_p + M_s)g, \quad Q_\alpha^{(we)} = (M_n d_{nv} + M_p d_{pv})g \sin \alpha + (M_n d_{nh} + M_p d_{ph})g \cos \alpha.$$

$$\text{Buoyancy Forces: } Q_\zeta^{(b)} = 0, \quad Q_\eta^{(b)} = -\rho_\omega V_g g, \quad Q_\alpha^{(b)} = \rho_\omega V_g d_G \sin \alpha, \quad (6)$$

Wind Forces: $Q^{(wi)}$ defined in Section 2.1.1

Tie Rod Forces: $Q^{(tr)}$ defined in Eqs. (26–33) of [3] (see also comments below and Appendix B)

Wave Forces: $Q^{(wa)}$ defined in Eqs. (47,48,51,52,54) of [3]

Hydraulic Drag Force: $Q^{(hy)}$ defined in Eqs. (45,46,49,50,53) of [3]

and finally the force (torque) in each surge, heave, and pitch direction is given by summing up each force component:

$$\begin{aligned} Q_\zeta &= Q_\zeta^{(we)} + Q_\zeta^{(b)} + Q_\zeta^{(wi)} + Q_\zeta^{(tr)} + Q_\zeta^{(wa)} + Q_\zeta^{(hy)}, \\ Q_\eta &= Q_\eta^{(we)} + Q_\eta^{(b)} + Q_\eta^{(wi)} + Q_\eta^{(tr)} + Q_\eta^{(wa)} + Q_\eta^{(hy)}, \\ Q_\alpha &= Q_\alpha^{(we)} + Q_\alpha^{(b)} + Q_\alpha^{(wi)} + Q_\alpha^{(tr)} + Q_\alpha^{(wa)} + Q_\alpha^{(hy)}. \end{aligned}$$

Here g is the standard acceleration of gravity; constants denoted by M , d and V (with subscripts) are wind-turbine geometry-dependent (effective) masses, distances between principal geometrical positions within the turbine, and volumes, respectively.

We do not present all the details for the "Tie Rod", "Wind", "Waves" and "Hydraulic Drag Forces" here to avoid bulky expressions. However, we choose to discuss some selective details of the platform modeling which are either principal (thus need to be emphasized) or when our implementation deviates from the Betti model baseline. Specifically, we clarify in Section 2.1.1 how the wind forces are computed by representing the wind turbine tower in terms of a series of cross-sections, each viewed as a point-wise element. In reference to the tie rod forces (also called mooring line forces), we follow the description of Eqs. (26–33) of [3] with the weight of the tie rods, λ_{tir} , which was not provided in [3], defined in Appendix B. **We also emphasize that the tie rod forces are nonlinear. These forces depend on mooring elongation and thus adapt to the nonlinearities of the Tension Leg Platform (TLP).**

Let us also make a couple of additional comments clarifying the dependence of the platform modeling, discussed in this Section, on other aspects of our overall modeling approach discussed in the following:

- We emphasize in Section 2.2 dependence of the wind forces on the rotor angular speed.
- The wind and wave forces, as well as the evolution of the position (surge and heave) and pitch of the FOWT, depend on the exogenous wind and wave turbulent signal, described in Section 2.3.

2.1.1 Aerodynamic Model: Wind Forces.

The aerodynamic model encapsulates the wind thrust and aerodynamic drag forces exerted on the system. The wind thrust is dissected into three components: the thrust acting on the tower, the nacelle, and the blade.

The thrust exerted on the tower and the nacelle is computed using the following equation:

$$e \in \text{tower, nacelle} : Q_e^{(wi)} = -\frac{1}{2}\rho C_e A_e v_e^2, \quad (7)$$

where ρ is the air density, C_e is the drag coefficient depending on the shape of the tower and nacelle which do not change with time, v_e is the velocity actually perceived by the tower and nacelle (as the structure is moving, thus accounting for corrections to the wind speed related to heave velocity, v_η , and the pitch rate ω), and A_e is the tower and nacelle swept area, respectively.

To compute the wind thrust acting on the blades, the Blade Element Momentum (BEM) approach is employed [?]. This approach, used extensively in the development of wind turbine aerodynamic models, divides the blade into several small parts and requires an appropriate choice of the number of sections to balance accuracy and calculation time. The medium-fidelity AeroDyn v15 software [?] is employed for the computation of blade element momentum which returns a thrust coefficient of the blade $C_t(\lambda, \beta)$, dependent on the tip speed ratio λ and the blade pitch angle β , both changing with time. This thrust coefficient is then incorporated to compute the wind (thrust) force

$$Q_{blade}^{(wi)} = -\frac{1}{2}\rho A_{blade} C_t(\lambda, \beta) v_{blade}^2, \quad (8)$$

with

$$\lambda = \frac{\omega_R R}{v_{blade}}, \quad (9)$$

where A_{blade} is the disc rotor area of the blade, ω_R is the rotor speed, and R is the rotor radius. The pitch angle β is set by the controller described in Section 2.5 and depends on time. Here in Eq. (8), the relative wind speed on blades $v_{blade} = v_w + v_\eta + d\omega \cos \alpha$ where v_w is the wind velocity and d is the distance from the center mass to the blade.

Finally, we sum up the wind thrust acting on each component of the wind turbine, thus arriving at

$$Q_\eta^{(wi)} = Q_{tower}^{(wi)} + Q_{nacelle}^{(wi)} + Q_{blade}^{(wi)}. \quad (10)$$

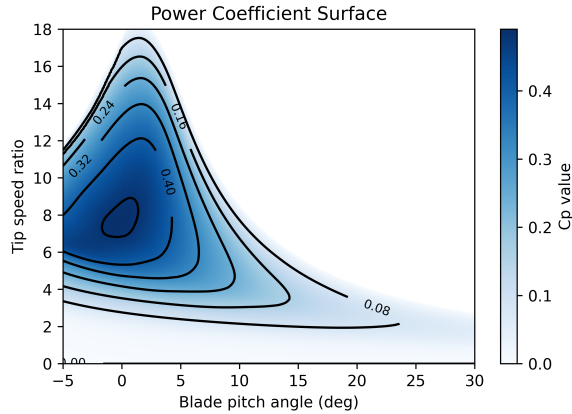


Figure 4: The power coefficient surface computed using NREL AeroDyn v15 software.

2.2 Drivetrain Model: The Rotating Part.

We follow the approach of [3?] and use a one-mass drivetrain model expressing dynamics of the transformation from the wind (aerodynamic) power to the electric power:

$$\dot{\omega}_R = \frac{1}{\tilde{J}_R} \left(\frac{P_A}{\omega_R} - \tilde{T}_E \right), \quad (11)$$

where ω_R is the rotor speed (angular velocity) of the blades/rotor considered, according to Fig. 3, to be one of the 7 state variables of the wind turbine. P_A in Eq. (11) is the aerodynamic power, computed according to:

$$P_A = \frac{1}{2} \rho C_p(\lambda, \beta) v_{blade}^3, \quad (12)$$

where v_{blade}^3 is the wind velocity at the blade (see discussion of the preceding subsection); $C_p(\lambda, \beta)$ is the power coefficient parameter, depending on the tip-speed ratio, λ , defined in Eq.(9) and on the blade pitch angle β , which is computed as an empirical function shown in Fig. 4 (adapted in this study from the NREL AeroDyn v15 software [?]).

The integrated electro-mechanical characteristics entering Eq. (11) are \tilde{J}_R – the overall inertia of the combined high-speed shaft, connected to the blades and rotated with the angular velocity ω_R ; ω_G – the angular velocity of the low-speed shaft connected to the electric system; and \tilde{T}_E – the resistant torque of the electric generator. The electro-mechanical characteristics are computed according to

$$\tilde{J}_R = J_R + \eta_G^2 J_G, \quad \tilde{T}_E = \eta_G T_E, \quad (13)$$

with an assumption of 100% efficiency in the generator. In the equation, the ratio of low-speed to high-speed angular velocities, $\eta_G = \omega_G / \omega_R$, is kept constant; J_R is the rotor (blade) inertia and T_E is the electric generator torque, both are subject to control – discussed in Section 2.5. (See Section II A of [3] for further details of the drivetrain part of the design.)

2.3 Model of Wind and Wave

Turbulent wind samples are generated using the NREL TurbSim v2.0 [?] software implementing the so-called Von Karman's model. (An exemplary input file is shown in Appendix C.) To generate wave samples we work with the Pierson–Moskowitz spectrum of the wave energy [9]. A comprehensive description of the setting is provided in Section II C of [3]. An exemplary temporal wind-wave sample, for the average wind speed of 20 m/s, is shown in Fig. 5.

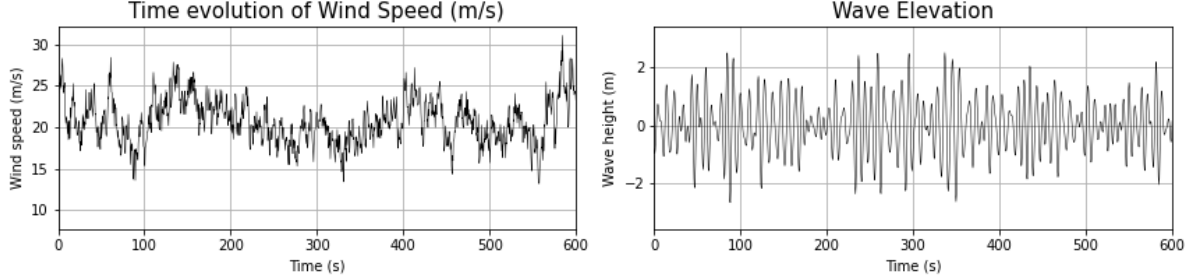


Figure 5: The wind profile with turbulence at average wind speed 20 m/s, and the wave profile generated using the Pierson–Moskowitz spectrum at reference wind speed 20 m/s

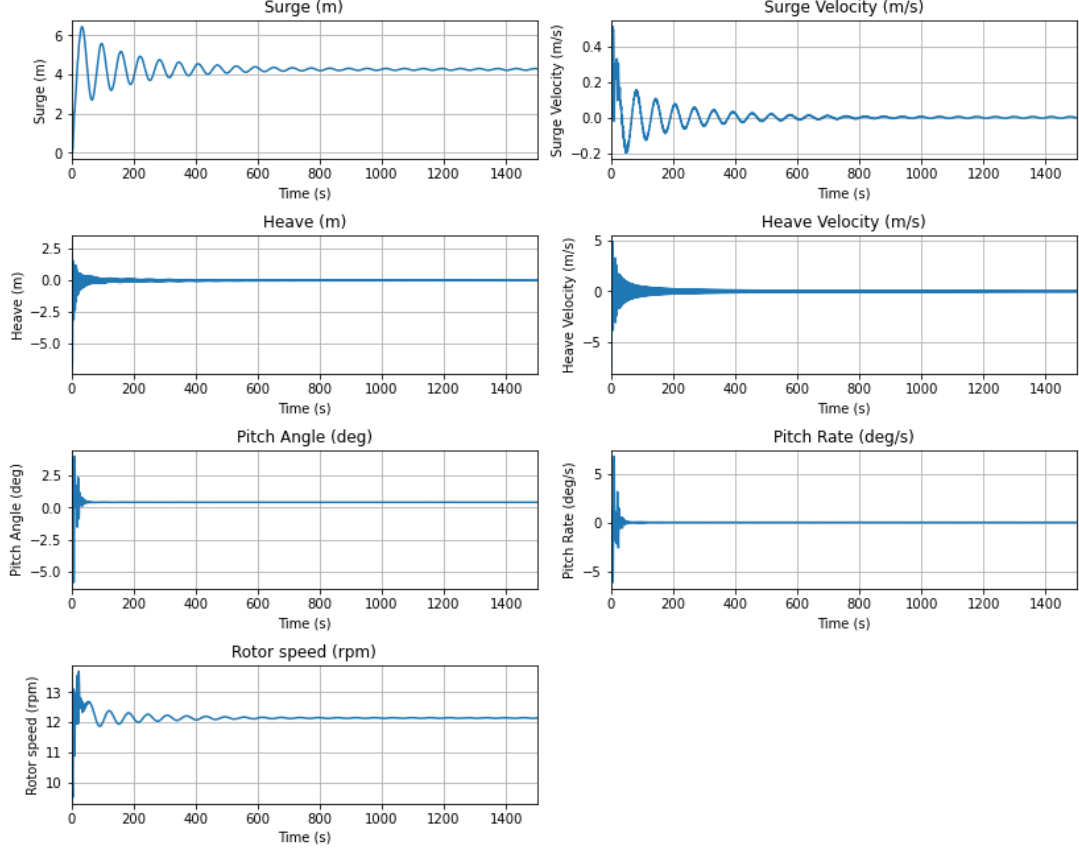


Figure 6: Results of simulations under constant wind at 11 m/s and no waves.

2.4 Steady State Verification

The steady-state verification process assesses the model's performance under static conditions. This verification involves executing simulations with constant, non-turbulent wind, and no wave. This validation step provides essential insights into the stability and reliability of the model, thus serving as a preliminary performance indicator prior to exposing the model to richer dynamic conditions. Notice, that the control inputs (blade pitch angle and generator torques), were fixed to constant in the steady state validation step.

Our first test, illustrated in Fig. 6, was conducted at the rated wind speed of 11.0 m/s (Region 2), with an initial condition close to the expected steady state. Under the rated operation condition, the blade pitch angle is maintained at 0 degree and the generator torque is set to the rated 43,093.55 N·m. The simulation results align well with the anticipated outcome. Notably, all six state variables and the rotor speed stabilize at static values in finite time, while the surge velocity, heave, heave velocity, and pitch rate remain zero. Table 1 presents the comparison of surge, and pitch offset between the Betthi model and the reference value from Table 2 of [5]. The results are close to the alignment values reported for this regime in [5]. Given the chosen control variables and environment setup, the expected rotor speed is equal to the rated rotor speed of 12.1 m/s, which is fully consistent with our findings.

	Betti's Model	Reference Value
Surge (m)	4.292	4.394
Pitch (deg)	0.415	0.438

Table 1: Comparesion of static state properties between Betti's model and reference value.

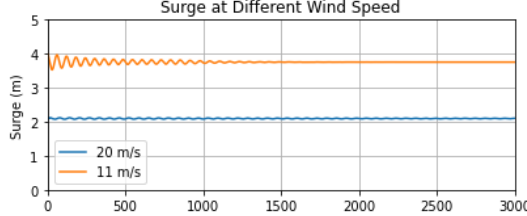


Figure 7: Surge displacement under constant wind at 20 m/s and no waves.

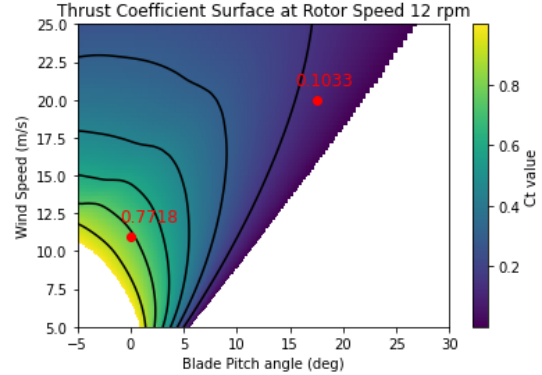


Figure 8: The thrust coefficient surface with rotor speed at the rated 12.1 rpm. The labeled red dots are the thrust coefficient on blades when operating at the rated rotor speed under 11 m/s and 20 m/s wind speed conditions.

Our second test was conducted at a constant wind speed of 20 m/s (a regime from Region 3). To maintain the rotor speed at the rated 12.1 rpm, the control variable blade pitch angle and the generator torque are set to 18° and the rated $43,093.55 \text{ N} \cdot \text{m}$ [4], respectively. Analysis of this case is documented in Fig. 7 where only surge positions are shown since the behavior of the remaining quantities mirrors those of Fig. 6 and aligns well with what is expected.

Fig. 7 compares the surge steady position operating under 11 m/s and 20 m/s constant wind conditions at the rated rotor speed. It is intriguing to observe that FOWTs operating with higher wind speeds exhibit smaller surge offsets. This observation implies that the net wind thrust acting on the structure is lower in higher wind speed conditions. To further explore this phenomenon, Fig. 8 presents the blade thrust coefficient surface - a parameter used to calculate the wind thrust acting on the blades C_t in Eq. 8, demonstrates the relationship between the blade thrust coefficient, wind speed, and blade pitch angle at the rated rotor speed of 12.1 rpm. As seen in the figure, an increase in the wind speed and blade pitch angle corresponds to a decrease in the thrust coefficient. The corresponding value of C_t when operating in 11 m/s is 0.7718 and 20 m/s is 0.1033. The corresponding points and values are also labeled in Fig. 8. Although the wind speed increases, the change of the blade pitch angle reduces the blade thrust coefficient more rapidly, finally leading to a reduced net thrust and, consequently, reduced surge offset. Fig. 9 shows the thrust curve versus wind speed which provides a more direct insight into the relationships. This phenomenon and its causes will be useful when explaining the extreme surge events in Section 3.2.1.

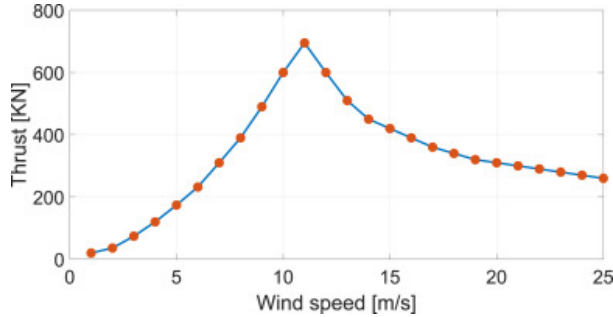


Figure 9: Thrust curve for the 5 MW NREL wind turbine. Taken from [?]

2.5 Implementation of the Blade-Pitch Controller

We examine a wind turbine operating in the so-called Region 3, as depicted in Fig. 1 of [3], which corresponds to a high wind speed regime when the wind turbine operates above the rated wind speed. We first follow the blade angle PI controller introduced in [4]. Then we multiply and tune the proportional and integration coefficients a_p and a_i in Eq. 17.

In this region, the generator maintains a constant power output, denoted as P_0 . Consequently, the resistive torque of the power generator, \tilde{T}_E , integral to the rotor dynamic equation Eq. (11), is inversely related to the rotor speed ω_R :

$$\tilde{T}_E = \frac{P_0}{\omega_G} = \frac{P_0}{\eta_G \omega_R}, \quad (14)$$

where η_G is a constant factor. A similar form applies to the aerodynamic torque \tilde{T}_A , which also influences Eq. (11), given by

$$\tilde{T}_A = \frac{P_A(\beta)}{\omega_R} = \frac{\rho C_2(\lambda, \beta) v_{\text{blade}}^3}{2\omega_R}, \quad (15)$$

where Eq. (12) is used, highlighting the functional dependence of the aerodynamic power, P_A , on the blade pitch angle β .

To achieve the control goal we change the blade pitch β in response to the observation of $\omega_R(t)$ and aim to stabilize it around its rated value, $\omega_0 = 12.1 \text{ rpm}$. We use a Proportional-Integral-Derivative (PID) controller, therefore introducing correction to β , $\beta \rightarrow \beta + \Delta\beta$, in response to the change in ω_R , where $\Delta\beta$ is a combination of terms which are linear in $(\omega_R(t) - \omega_0)$ (proportional), linear in $\int_0^t \omega_R(t') dt' / t$ (integral), and linear in $\dot{\omega}_R(t)$ (derivative):

$$\Delta\beta(t) = K_p \eta_G (\omega_R(t) - \omega_0) + K_i \int_0^t \eta_G (\omega_R(t') - \omega_0) dt' / t + K_d \eta_G \dot{\omega}_R(t). \quad (16)$$

Gain parameters of the PID controller are fixed consistently with the goal – to stabilize the right-hand side of Eq. (11). We follow here the strategy of [?] (see also [?] and [?]) in choosing the K_p and K_i gain parameters:

$$K_p = a_p \frac{2\tilde{J}_R \omega_0 \zeta_\phi \omega_\phi}{\eta_G |\partial_\beta(P_A(0))|} \frac{\beta_k}{\beta_k + \beta}, \quad K_i = a_i \frac{\tilde{J}_R \omega_0 \omega_\phi}{\eta_G |\partial_\beta(P_A(0))|} \frac{\beta_k}{\beta_k + \beta}. \quad (17)$$

Here, a_p and a_i are detuning parameters which will be defined next. the constant parameters $\omega_\phi = 0.6 \text{ rad/s}$, $\zeta_\phi = 0.7$ ("natural frequency" and the damping ratio) and $\beta_k = 6.302336 \text{ rad}$ were set according to [4], where the sensitivity of the aerodynamic power to blade pitch angle $\partial_\beta P_A$ was calculated for the NREL offshore 5-MW baseline wind turbine by performing a linearization analysis with AeroDyn software at a number of steady, uniform wind speed profile at the rated rotor speed while producing the rated mechanical power.

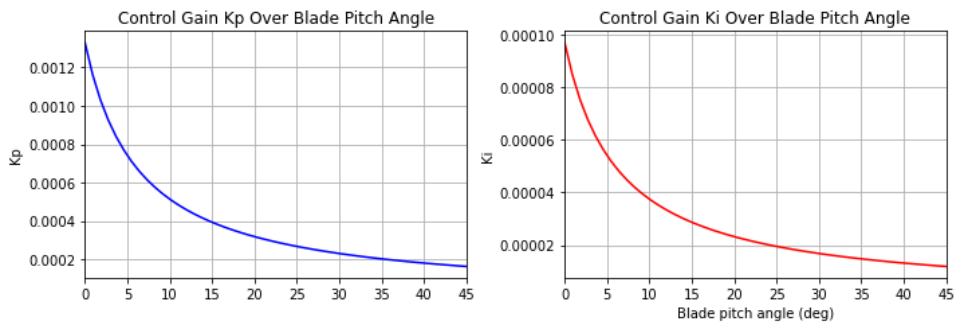


Figure 10: Control proportion and integral gains Control gain coefficients C_p (proportional) and C_i (integral) vs the blade pitch angle β .

We set a_p and a_i in Eq. (17) empirically through the following procedure:

1. Set $a_i = 1$. While simulating the case of steady wind and no waves, increase a_p from zero till the value for which the PI controller (without the D-part) loses its stability. Then half the value. We arrived at $a_p = 0.0765$.
2. To fine-tune the integral gain we conduct simulations under typical stochastic wind and wave conditions, retaining the predetermined proportional gain and continuing to work with the PI (and not yet PID) setting. (We remind that the integral gain's primary role is to eliminate the steady-state error by summing up past discrepancies between the actual and set values over time, which

the proportional gain alone cannot fully achieve.) We start with $a_i = 1$, and calculate the average rotor speed where the averaging is over time (25 min). We adjust a_i until the average becomes close to the rated rotor speed of 12.1 rpm. We arrived at $a_i = 0.013$.

The dependence of the resulting control gain coefficients of the fine-tuned PI controller on the blade pitch angle is illustrated in Fig. 10.

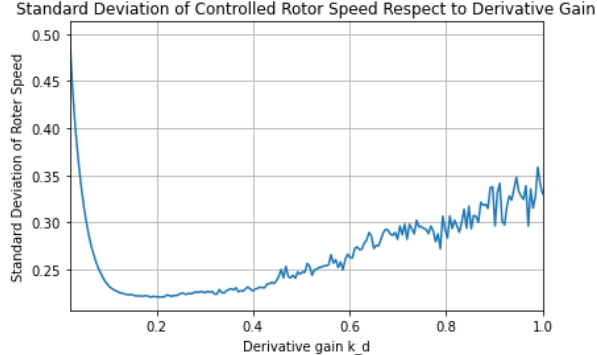


Figure 11: Turning K_d : Standard deviation of the rotor speed as a function of the derivative gain K_d .

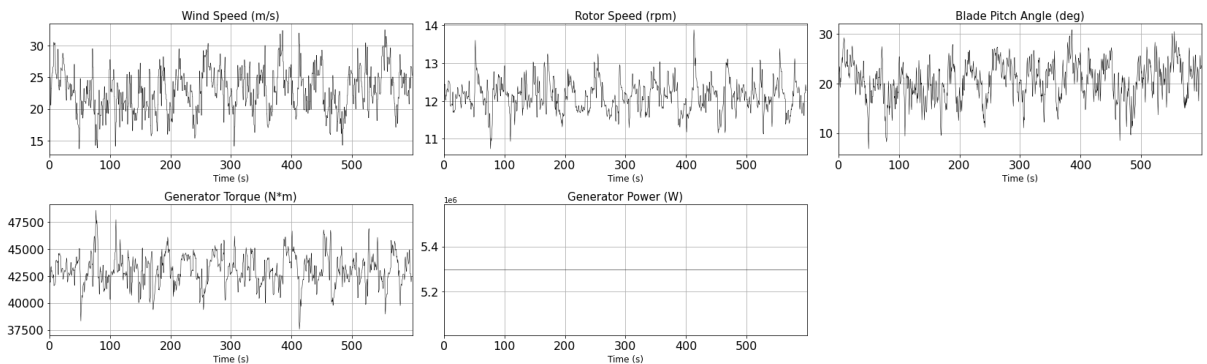


Figure 12: Properties of the drivetrain.

Setting up the differential part of the PID controller becomes our next step. The role of the derivative gain is to minimize overshoot and attenuate amplitude. Unlike proportional and integral gains, the derivative gain is set to a constant. Ideally, the derivative gain should yield the lowest standard deviation of rotor speed throughout the simulation. To achieve this goal we study the dependence of the standard deviation of the rotor speed (where averaging is over time) on the derivative gain, ranging from 0.02 to 1. The result is shown in Fig. 11. We observe a clear minimum at $K_d = 0.1874$.

Finally, we limit the maximum rate of the blade-pitch angle change to 8 deg/s, also allowing the range 0 – 90° for the blade-pitch angle.

The performance of the resulting PID transformer is illustrated in Fig. 12. The figure presents the control performance in Region 3, showing the blade pitch angle, generator torque, rotor speed, and power production. It is noteworthy that the controller adheres to a constant power strategy.

3 Markov Chain Monte Carlo Simulation

The Markov chain Monte Carlo (MCMC) analysis was performed by analyzing the large dataset obtained from simulations under stochastic wind and wave perturbations. This analysis focuses on the probability and distribution of occurrence of rare events, such as negative damping [?] and extreme displacements or accelerations. The simulation was carried out in Region 3, characterized by high wind velocities, and incorporated the Blade-Pitch PID controller described in Section 2.5.

This Section commences with a synthesis of our simulation outcomes in Section 3.1 and an analysis of the resulting data distribution in Section 3.2 where we discuss a curated set of trajectories derived

from the MCMC simulations. Our approach to the curated set of trajectories, also called instantons, is twofold: we initially identify trajectories that exhibit noteworthy behaviors and subsequently delve into interpreting and elucidating the underlying mechanisms of these phenomena.

3.1 Simulation Results Overview

We conducted 10,000 individual simulations, each with a duration of 1,500 seconds. These simulations included stochastic turbulence fluctuations, generated by TurbSim [?], along with stochastic wave patterns, under an average wind velocity of 20 m/s. We use “B” mode for turbulence characteristic in Turbsim (see Appendix. C) resulting in a turbulence intensity of 14.42%. The transient at the beginning of each sample is discarded to avoid bias due to the selection of initial value. Fig. 13 presents the probability density function (PDF), which depicts the overall distribution of individual states (gray) and also the distribution of the extreme values minima (blue) and maxima (red). With regards to the latter, each trajectory contributes one maximum and one minimum value to the PDF, representing the most extreme states observed within its 1,500-second interval.

This analysis of extreme statistics is crucial for understanding the turbine’s anomalous responses to environmental forces. Notably, the impact of extreme events, unless specifically isolated, remains obscured within the tails of the standard probability distribution, which is depicted in gray in Fig. 13. It is also important to note that the typical values of these extremes – near the peaks of the blue and red distributions in Fig. 13 – also fall within the tail of the standard event distribution.

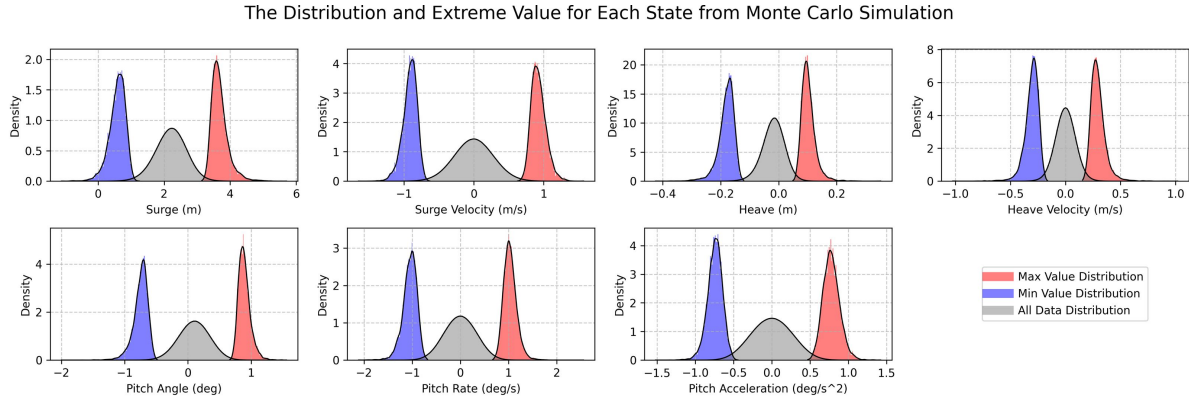


Figure 13: Probability Density Function shows the distribution of each state, and the distribution of extreme value at every time step.

3.2 Extreme Events Analysis

In this Subsection, we discuss the outcomes via visualizations/figures derived from our MCMC simulations. Our focus is on delineating distinct scenarios/events that exhibit anomalous behaviors. Each scenario is characterized by temporal evolution of a set of nine parameters: wind speed, surface wave elevation (measured at the average surge position), surge, surge rate, heave, heave rate, pitch angle, rate of pitch angle change, and pitch angle acceleration or rotor speed. We chart the temporal progression of these parameters to illustrate their dynamic behavior. Additionally, our figures integrate a percentile range, along with the maximum and minimum values at each time of the evolution, collated from all MCMC simulations. This inclusion aims to enrich the graphical depiction and facilitate a more intuitive understanding of the scenarios and comprehension of the data.

3.2.1 Extreme Surge Events

This Subsubsection examines events characterized by significant variations in surge (platform elevation) and its rate of change.

The first two events of this type – distinct due to an anomalously large value of the surge observed during their evolution – are shown in Fig. 14 and Fig. 15. We observe that these events occur when the wind drops suddenly – from the typical value of 20 m/s to an anomalously low value of 10 m/s. We conjecture, based on the collocation of the two observations in time that the latter (drop in the wind)

causes a series of mechanical responses in the rotor system which leads to the former (anomaly in the surge and in the surge's rate).

To further investigate the role of the controller in these events, we show the evolution of these characteristics in the low panel of Fig. 14 and Fig. 15. Normally stable, the rotor speed exhibits a rapid decline in response to the sudden decrease in wind speed. We hypothesize that the decline is due, at least in part, to the limitations of the rotor's blade pitch angle controller which has limitation – it can only adjust the blade pitch angle at a maximum rate of $8^\circ/\text{sec}$ and the blade pitch angle cannot be smaller than 0° . This implies that the controller's response to rapid changes in wind speed is limited, leading to a sharp decrease in rotor speed.

This process is further complicated by the system's net thrust sensitivity to changes in the blade pitch angle explained in Section. 2.4. As the wind speed decreases, the controller reduces the blade pitch angle. This action, paradoxically, increases the net wind thrust on the system, causing the system to be pushed further by the wind. This phenomenon is evident in the surge offset increase and the rapid decrease in rotor speed following the wind speed change, as depicted in the Fig. 14 and Fig. 15. (Refer to the lower right panel of Fig. 16 for the legends used in Figs. 14,15.)

Furthermore, during the minute following the anomalous surge the rotor speed continues to fall below its rated speed, and the controller adjusts the blade pitch angle at its maximum rate in an effort to recover rotor speed. Concurrently, the wind speed begins to recover, leading to a rapid increase in rotor speed, much faster than expected. This results in a significant overshoot. Additionally, the over-correction of the blade pitch angle reduces the net wind thrust on the system, causing the system to swing back more rapidly under the tension of the ropes. However, at this stage, once the wind speed returns to its normal pattern, the controller successfully stabilizes the rotor speed without further overshooting, allowing the system to return to its normal operational pattern.

We need to emphasize here that at this initial study of rare events, we intended to only study Region 3 and the model lacks the generator torque controller in Region 2 and below. In theory, based the wind model we use, we only produce wind signal in Region 3 which is above the rated wind velocity of 11 m/s. However due to the nature of stochastic process, we can not absolute avoid the wind signal reaches Region 2, and because this surge fluctuation is mostly due to the blade pitch angle controller, we believe this analysis is still valuable in the context.

In this initial study of FWT rare events, we specifically focus on Region 3. Our model intentionally omits the generator torque controller for Region 2 and below, as the wind model theoretically generates wind signals exclusively for Region 3. However, due to the stochastic nature of the process, occasional wind signals may drop into Region 2. Since these surge fluctuations are primarily influenced by the blade pitch angle controller, we believe this analysis remains valuable within this context.

Also, it is worth noting that the surge velocity seen in Fig. 14 and Fig. 15 is not affected by this series of events and remains normal.

The third event showing an anomalously large surge is shown in Fig. 16. Here we observe that the anomaly in surge (and its rate) is triggered by a wave-related anomaly. Unlike the events shown in Figs. 14,15 the wind event does not result in any anomaly in the rotor's speed.

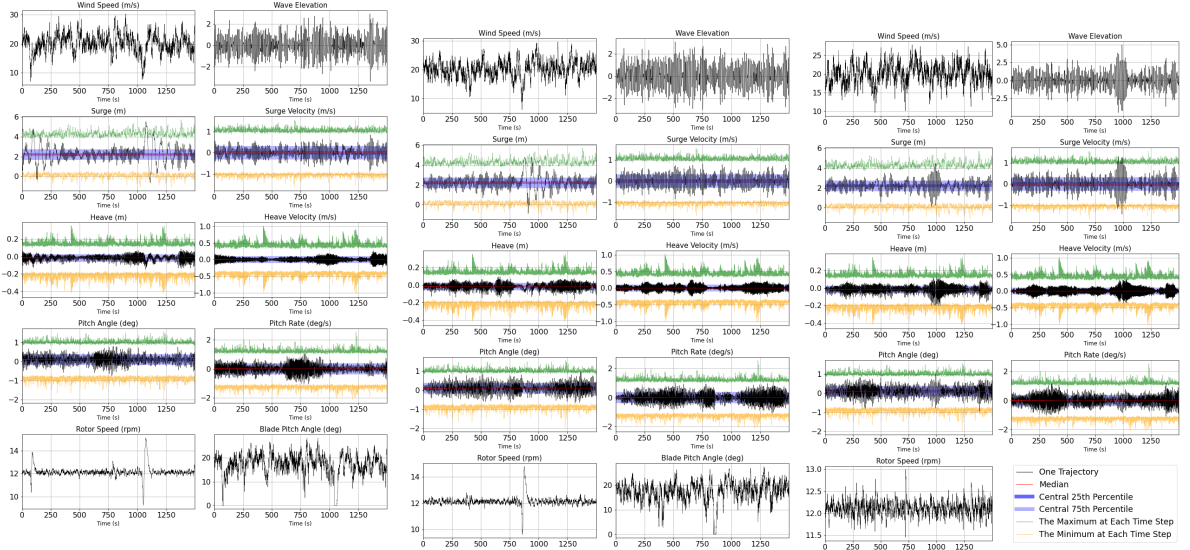


Figure 14: Surge fluctuations induced by wind activities and the controller (0 - 500 seconds and 1000 - 1500 controller (800 - 1200 seconds).

Figure 15: Surge fluctuations induced by wind activities and the controller (0 - 500 seconds and 1000 - 1500 controller (800 - 1200 seconds).

Figure 16: Surge fluctuations induced by wave activities (900 - 1100 seconds).

3.2.2 Wind-Induced Short- vs Long-Correlated Anomalies in Wind Turbine Responses

Figs. 17 to 19 depict scenarios where surge anomalies—specifically, significant elevations of the wind-turbine platform exceeding 8 meters—are linked to wave anomalies, similar to the previously discussed case. However, these events also exhibit significant concurrent responses in heave and pitch, differing from the previously mentioned example.

Specifically, Fig. 17 captures a sharp oscillatory response in the platform’s movement during the encounter with large waves, noticeable in the interval of 400 to 600 seconds. Here we observe that the effects on heave and pitch are short-lived, with both parameters rapidly returning to stable conditions post the intense wave activity.

This scenario exemplifies an anomaly with a short ‘memory span’, categorized as ‘short-correlated’, where monitored characteristics return to normal within approximately 200 seconds.

In contrast, the scenario in Fig. 18 presents a ‘long-correlated’ anomaly, characterized by prolonged higher wave surface elevations lasting between 600 and 800 seconds. We coin it as ‘long-correlated’ anomaly. Notably, in this long-correlated scenario, despite the large wave amplitudes, the maximum deviations in heave and pitch are relatively lower. Furthermore, unlike in the case of the short-correlated scenario, the platform in the scenario of Fig. 18 fails to re-establish stability after the waves subside to their regular patterns. Instead, we witness an extended duration of notable oscillations, lasting approximately 700 seconds, with pitch parameters being especially affected.

Therefore, we characterize the scenarios illustrated in Fig. 17 and Fig. 18 as short-correlated and long-correlated, respectively.

Moreover, our analysis contrasting short versus long correlations demonstrates that large waves, while they induce a significant instantaneous increase in platform elevation, do not invariably lead to prolonged fluctuations. As demonstrated in Fig. 19, the platform experiences a substantial wave, evidenced by an 8-meter drop at the 400-second mark (a magnitude comparable to the event in Fig. 18). However, in this case, the system quickly regains stability, doing so in approximately 100 seconds.

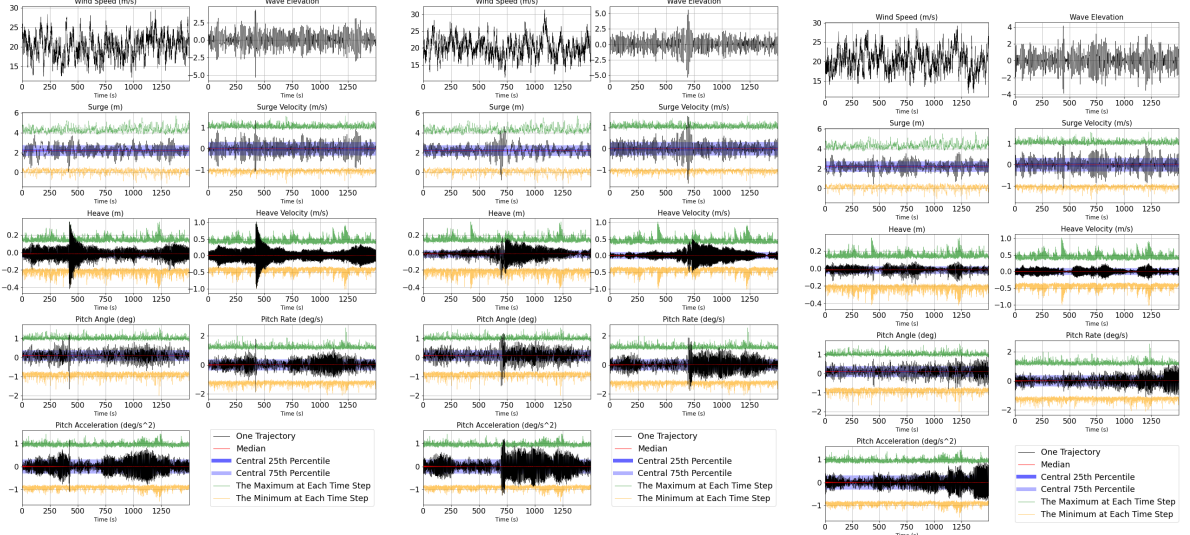


Figure 17: Fluctuations induced by wave activities, short-lived (400 - 600 seconds).

Figure 18: Fluctuations induced by wave activities, long-lived (700 - 1400 seconds).

Figure 19: Substantial wave activities with stable platform (400 - 500 seconds).

3.2.3 Characterizing Subtle Wave Influences on Prolonged Pitch Dynamics

Fig. 20 through 22 depict a noteworthy scenario where, despite wave amplitudes being under 3 meters, there is a notable increase in pitch-related dynamics, including amplitude, rate, and acceleration, which persist for an extended period. This prolonged activity is particularly fascinating due to its lack of correlation with significant wave or wind events.

While the extent of these pitch variations may be less than those encountered in conditions with larger waves, as discussed earlier, their persistent nature, and especially the acceleration, raises questions about their effect on structural integrity. This highlights the need for a thorough investigation. To better illustrate this, we present three illustrative cases.

Additional insights for the scenarios depicted in FIG 20 through 22 are provided by FIG 23 through 25 and FIG 26 through 28, which display the frequency spectra of the waves and wind generated by Fast Fourier Transform (FFT), respectively. In these figures, the blue and red curves represent calm and anomalous conditions.

A comparative analysis of these two sets of figures reveals a consistency in the wind frequency spectra across all three cases, in contrast to the distinctly different wave frequency spectra. This observation suggests that wind factors may play a more substantial role in the documented pitch behavior.

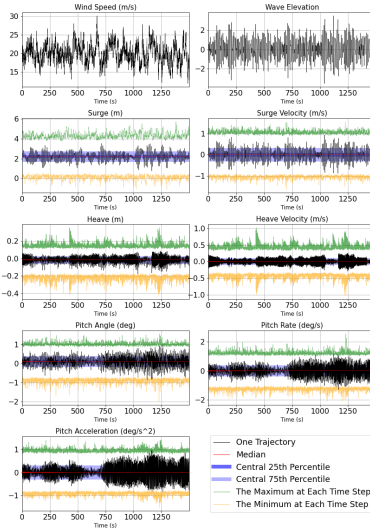


Figure 20: Fluctuations in pitch with no significant wave or wind activity (700 - 1500 seconds).

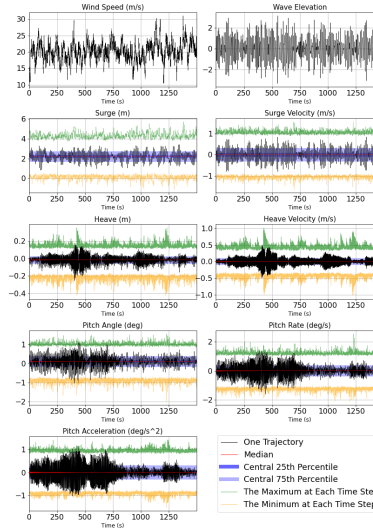


Figure 21: Fluctuations in pitch with no significant wave or wind activity (0 - 700 seconds).

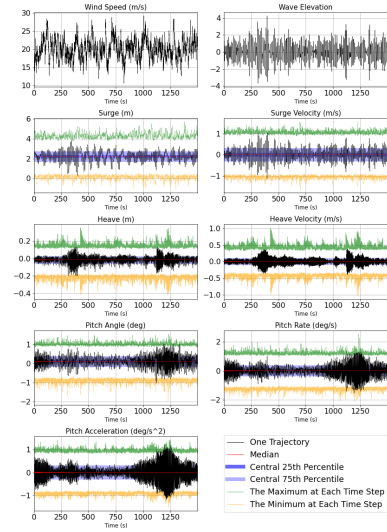


Figure 22: Fluctuations in pitch with no significant wave or wind activity (1000 - 1400 seconds).

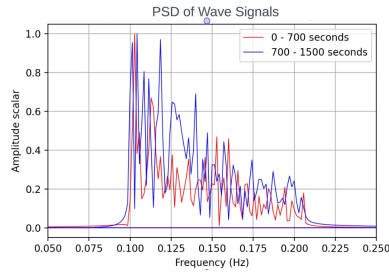


Figure 23: The Power Spectral Density (PSD) of wave signals for Fig. 20.

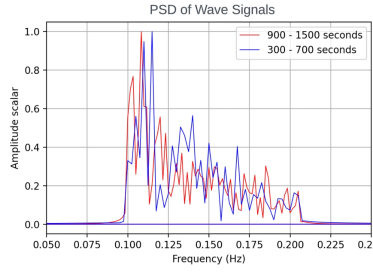


Figure 24: The Power Spectral Density (PSD) of wave signals for Fig. 21.

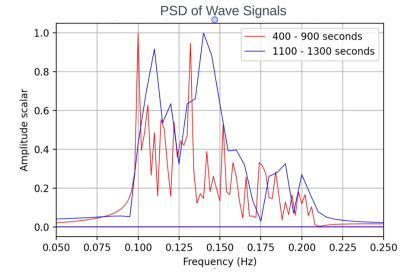


Figure 25: The Power Spectral Density (PSD) of wave signals for Fig. 22.

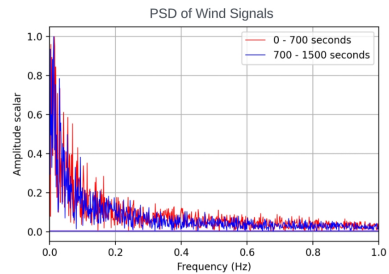


Figure 26: The Power Spectral Density (PSD) of wind signals for Fig. 20.

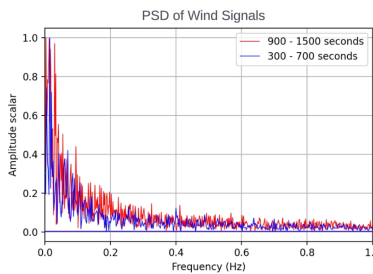


Figure 27: The Power Spectral Density (PSD) of wind signals for Fig. 21.

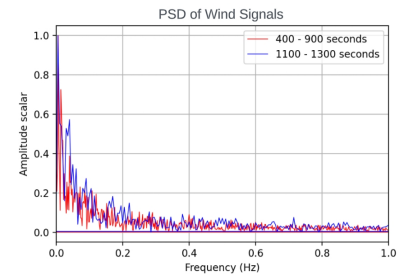


Figure 28: The Power Spectral Density (PSD) of wind signals for Fig. 22.

To further investigate the long-correlated anomalies, we embarked on a series of controlled simulations. Initially, we retained the same wind conditions as in our previous experiment but altered the wave patterns. This was done to assess whether the observed anomalies persisted under these new wave scenarios. Subsequently, we inverted the experimental setup: we kept the wave patterns constant while varying the wind conditions. This approach allowed us to examine the impact of wind variations on the anomalies.

To ensure the reliability of our findings and mitigate any potential biases, each configuration was tested multiple times. However, for brevity and clarity in presentation, only one representative trial per test is depicted in the figures. Fig. 20 through 22 illustrate three distinct events. We conducted the test for each of these events, and the results are detailed in the following paragraph.

Long Correlated Tests - Same Wave Profile: Fig. 29 through 31 illustrate the results from tests conducted under identical wave conditions, but with varying stochastic wind inputs. In these three independent scenarios, there were no discernible similarities in the behavior of the anomalies. This lack of consistency suggests that the wind variations did not produce a uniform anomaly pattern.

In addition, Fig. 32 through 34 show the outcomes from experiments using a constant wind profile paired with the same wave conditions. Similar to the previous tests, these scenarios also failed to exhibit consistent anomaly patterns.

These observations underscore that changing the wind input does not lead to similar anomaly behaviors in the tested events.

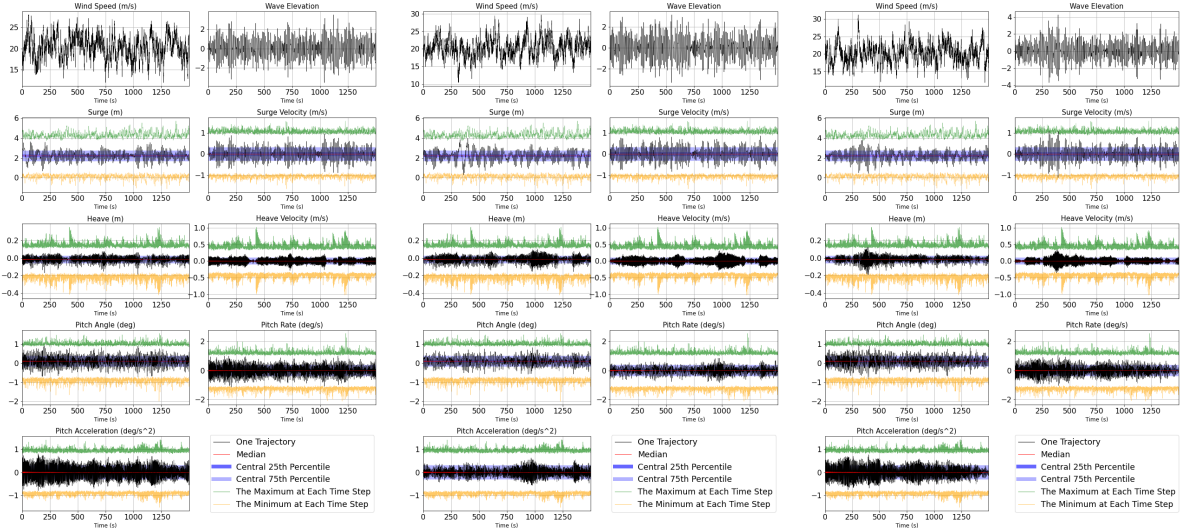


Figure 29: Same wave but different instance for Fig. 20).

Figure 30: Same wave but different instance for Fig. 21).

Figure 31: Same wave but different instance for Fig. 22).

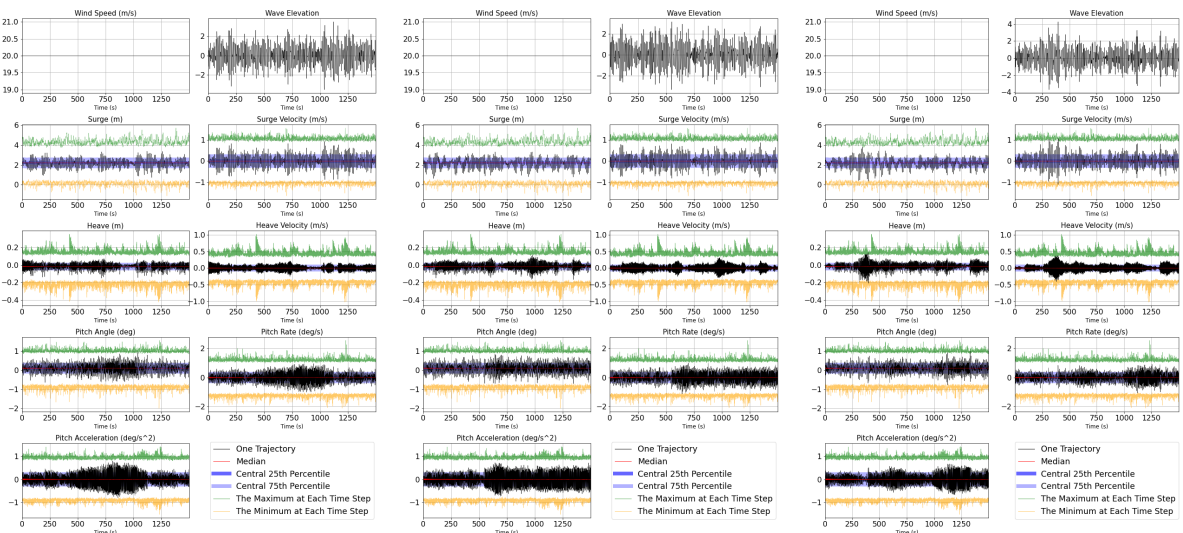


Figure 32: Same wave but constant instance for Fig. 20).

Figure 33: Same wave but constant instance for Fig. 21).

Figure 34: Same wave but constant instance for Fig. 22).

Long Correlated Tests - Same Wind Profile: FIGs (35 through 37) display the outcomes of experiments conducted with a consistent wind profile but varying stochastic wave conditions. These tests, focusing on pitch characteristics such as position, velocity, and acceleration, revealed a notable yet consistent anomaly pattern across all scenarios. This pattern persisted despite variations in amplitude. When coupled with the disappearance of anomalies under different wind conditions, these results strongly suggest that wind is the predominant factor influencing the long-term anomalous pitch behavior.

To further explore this hypothesis, we conducted additional tests for each event using the same wind conditions, but in the absence of waves (still water conditions). The results, as shown in Figs. 38 through 40, confirmed the persistence of the anomalous pitch patterns even in still water. This evidence leads us to conclude that wind plays a primary role in these long-term correlated anomalous pitch events. However, it is also apparent that certain wave conditions, which require further identification and analysis, might amplify these fluctuations. Additional research is needed to fully understand the interplay between wind and wave conditions in these phenomena.

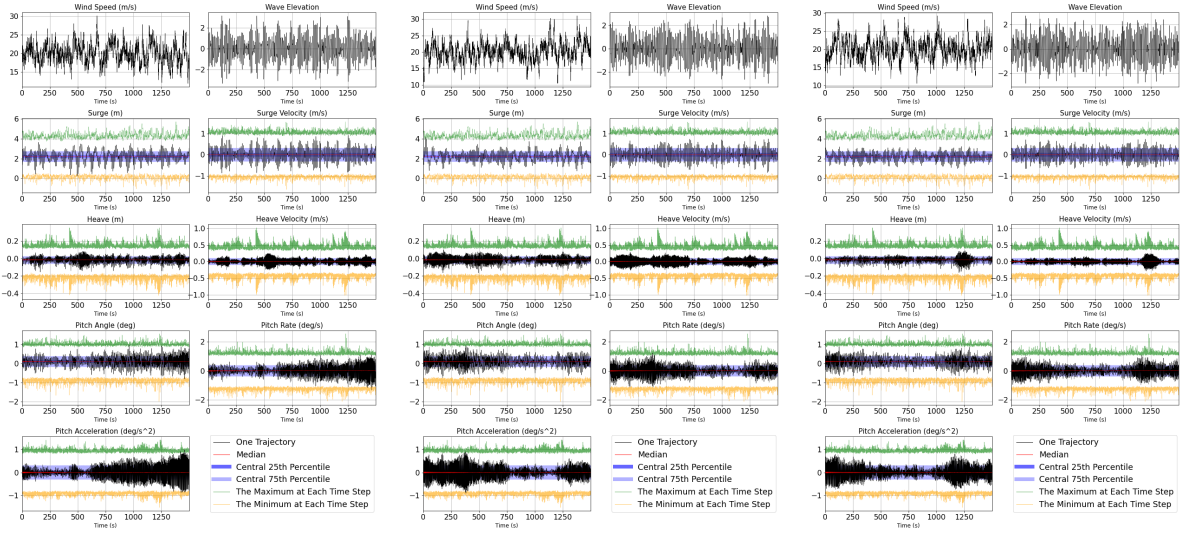


Figure 35: Same wind but different wave instance for Fig. 20).

Figure 36: Same wind but different wave instance for Fig. 21).

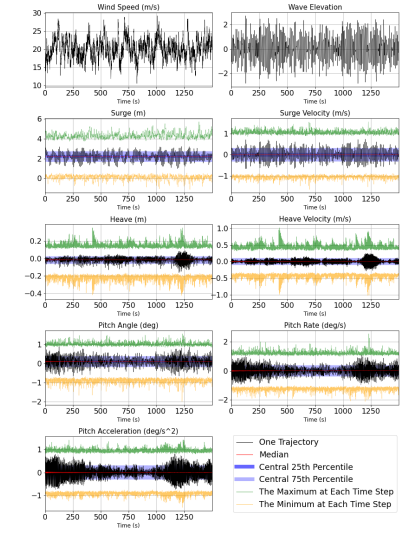


Figure 37: Same wave but different wind instance for Fig. 22).

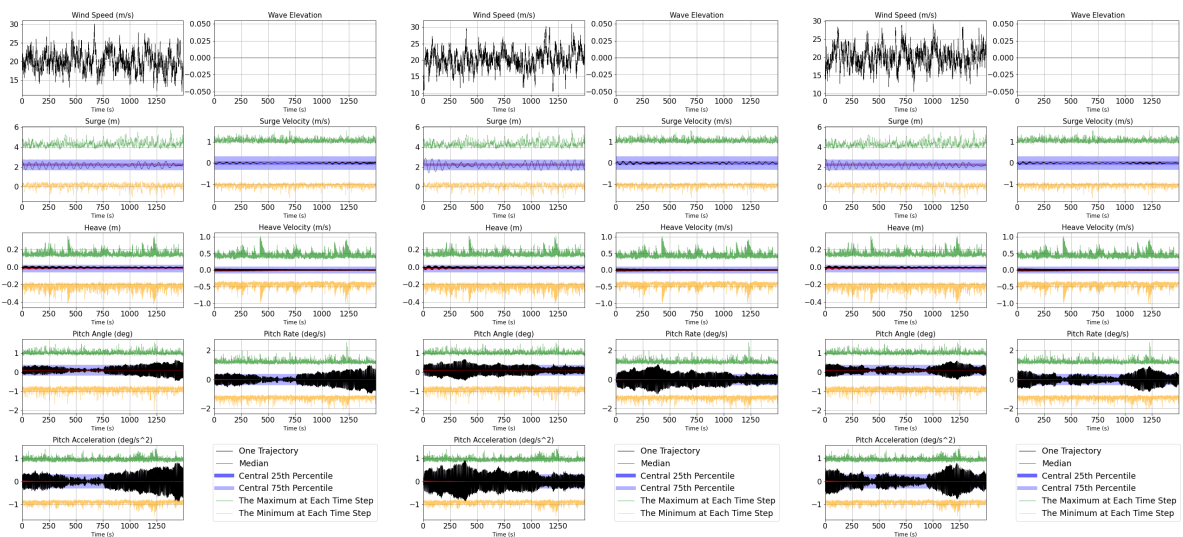


Figure 38: Same wind and no wave for Fig. 20

Figure 39: Same wind and no wave for Fig. 21

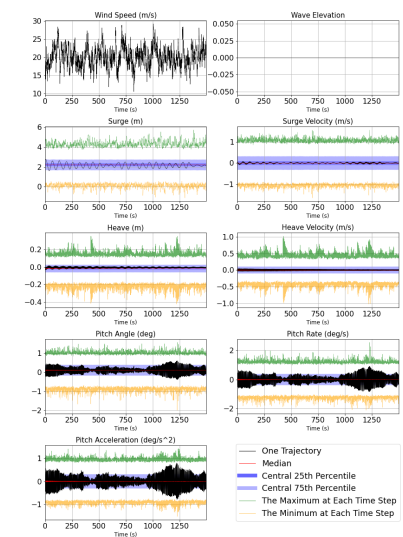


Figure 40: same wind and no wave for Fig. 22.

3.2.4 Are Anomalies in Heave and Pitch Collocated?

We are also interested in determining whether events related to pitch and heave are correlated. Fig. 41 presents a binned scatter plot over all trials and over all the times that elucidates the relationship between heave and pitch. In this analysis, the domain of heave is equally divided into 100 intervals. Each point in the scatter plot denotes the average pitch corresponding to each heave sub-interval, culminating in a total of 100 scatters. The observed horizontal trend in the plot indicates a negligible correlation, suggesting that pitch and heave events might be independent of each other.

Furthermore, we delve into the potential relationship between extreme events in heave and pitch. Fig. 42 illustrates the distribution of pitch values at instances of extreme heave, alongside the distribution of heave at moments of extreme pitch, further delineated by percentile regions. Notably, the PDFs for both pitch and heave display a resemblance to the patterns observed in Fig. 13. Additionally, the distributions corresponding to maximum and minimum thresholds overlap significantly. The evidence implies that extreme occurrences in heave do not necessarily correspond to extreme events in pitch and vice versa. Therefore, we conclude that events related to heave and pitch are predominantly independent.

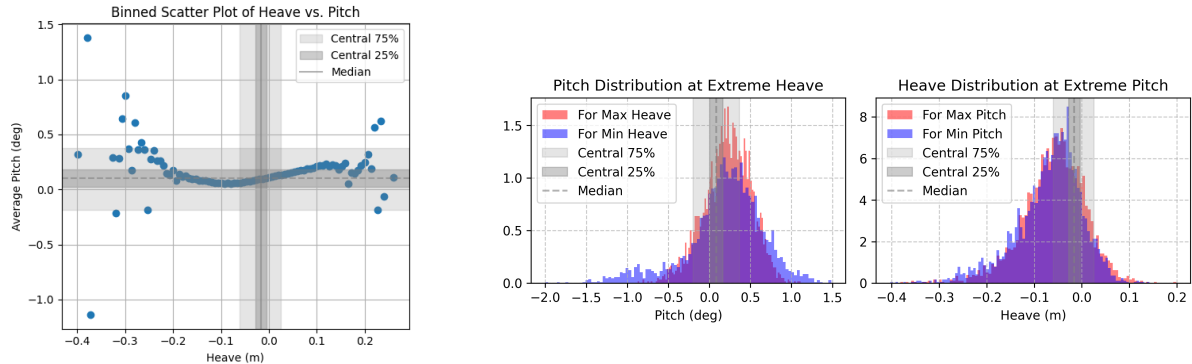


Figure 41: The binned scatter plot shows the correlation between heave and pitch.

Figure 42: PDFs shows the heave distribution at extreme pitch, and pitch distribution at extreme heave

4 Conclusions

This study, employing an extensive Markov Chain Monte Carlo (MCMC) simulation approach involving 10,000 individual runs, has provided significant insights into the behavior of Floating Offshore Wind Turbines (FOWT) under stochastic wind and wave conditions. Particularly, it focused on high wind velocity scenarios in Region 3, integrated with a Blade-Pitch PID controller. The emphasis was on the occurrence and characterization of rare events, with a comprehensive analysis to understand their causation.

Note that we chose to work with the reduced model of a wind turbine previously introduced in [3], which we tuned to be approximately consistent with a high-resolution offshore wind turbine NREL 5MW model [4]. The Betti model, with our custom parameter tuning, met our needs due to its simplicity, allowing us to code it ourselves. This was crucial as our primary focus was on using MCMC analysis to explore rare events impacting pitch, heave, and surge. Our aim was to understand the causative factors of these anomalies, which necessitated a white-box model like Betti's, rather than a more complex high-resolution or black-box model.

Working with the adapted Betti model, we identified and meticulously analyzed various scenarios that exhibited anomalous behaviors. A key observation was extreme surge events characterized by significant variations in surge and its rate of change, especially in response to sudden drops in wind speed. These findings are critical for understanding the dynamic response of FOWTs and for improving controller designs.

Anomalies were categorized into short-correlated and long-correlated types. Short-correlated anomalies, typically induced by large waves, were observed to quickly revert to normal behavior. Conversely, long-correlated anomalies involved prolonged oscillations, especially in pitch configurations, where the cause was not immediately apparent.

Through targeted control variable tests, we isolated the factors contributing to these long-correlated anomalies. These tests, which involved systematic alterations of wind and wave conditions, clearly demonstrated that wind is the primary factor driving these long-term anomalous pitch behaviors. This was particularly evident in scenarios void of wave activity. Furthermore, the interaction between specific wave conditions and wind was found to amplify the turbine's anomalous behavior under certain circumstances.

The insights gained from this study underscore the complex interplay between wind and wave conditions in influencing FOWT dynamics. They highlight the need for advanced control strategies and robust design considerations that can accommodate these intricate environmental interactions.

This study marks a crucial initial step in the comprehensive reliability analysis of Floating Offshore Wind Turbines (FOWT). It highlights the importance of developing methods to identify wind and wave sequences that lead to significant anomalies in surge, pitch, and heave, particularly those that persist. Our next step is to develop more efficient sampling approaches, specifically targeting events of special concern.

In the second paper of this series (work in progress), we plan to present further developments of the model, including a more realistic representation of the large-scale component of wind. Additionally, we aim to enhance the bootstrap MCMC approach by developing an importance sampling method, which leverages critical samples extracted from the initial MCMC. This importance sampling will then be made adaptive to improve efficiency.

Acknowledgments

We extend our thanks to Criston Hyett, whose insightful discussions and valuable suggestions were instrumental throughout this work. Additionally, we acknowledge the support provided to YL during his summer internship under the guidance of MC. This opportunity, made possible by the REU program at the University of Arizona, was funded by the "NSF/RTG: Applied Mathematics and Statistics for Data-Driven Discovery" project, to which we are grateful. ChatGPT was used to proofread the paper.

A Coordinate System Transformation

A.1 Surge and Pitch

We first of all would like to emphasize that the direction of surge and pitch used in [3] is opposite to the direction used in the paper which was adapted from RCCS [5]. To transfer between the two coordinate systems, we simply negate offsets for surge and pitch.

A.2 Heave

In [3], the vertical axis points downward, and the heave position is measured at the center of weight of the platform and of the tower (CS). Conversely, in the RCCS, the vertical axis points upward and the heave position is defined as zero at the stationary point. Therefore, to ascertain the heave position in RCCS, one needs to determine the relative position of the CS within the RCCS. The center of weight and relative position of the center of the platform (PS) and tower (TS), as provided in [3] and [5], are illustrated in Fig. 43. Subsequently, the position of the CS can be calculated by determining the center of mass. This position is -37.55 m . Finally, we use Eq. (18) to get the heave position in RCCS.

$$\eta_{RCCS} = 37.55 - \eta \quad (18)$$

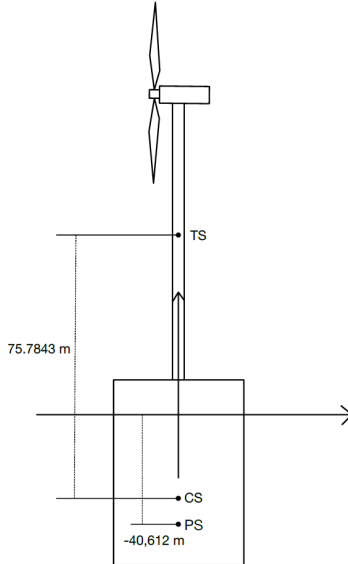


Figure 43: The relative distances to compute the position of CS.

B Weight Contribution of Tier Rod Lines

In [3] the net contribution of weight and buoyancy of the mooring lines is described by Eqs. (28–30) dependent on the parameter λ_{tir} , measured Newtons per meter (N/m), and once multiplied on the original (that is not under stress) tie rod length gives the combined effects of weight and buoyancy. Specifically, contributions of the weight and buoyancy terms to λ_{tir} are

$$\lambda_{tir} = \mathbf{w}_{tir} - \mathbf{b}_{tir}, \quad \mathbf{w}_{tir} = \lambda_l g, \quad \mathbf{b}_{tir} = \rho_w g(\pi r_l^2), \quad (19)$$

where λ_l is the mass density of the rod per length, ρ_w is the water density, and r_l is the rod radius. All the tie rod parameters are taken from [5].

C TurbSim Input Example

```
--TurbSim v2 (OpenFAST) Input File-----
for Certification Test #5 (SMOOTH Spectrum, formatted FF files, Coherent Structures).

-----Runtime Options-----
False Echo - Echo input data to <RootName>.ech (flag)
-187725731 RandSeed1 - First random seed (-2147483648 to 2147483647)
-1847245323 RandSeed2 - Second random seed (-2147483648 to 2147483647) for intrinsic pRNG, or an alternative pRNG: "RanLux" or "RNSNLW"
False WrBHHTP - Output hub-height turbulence parameters in binary form? (Generates RootName.bin)
False WrFHHTP - Output hub-height turbulence parameters in formatted form? (Generates RootName.dat)
True WrADHF - Output hub-height time-series data in Aerodyn form? (Generates RootName.hh)
False WrADFF - Output full-field time-series data in TurbSim/AeroDyn form? (Generates RootName.bts)
False WrBLFF - Output full-field time-series data in BLADED/AeroDyn form? (Generates RootName.wnd)
False WrADTWR - Output tower time-series data? (Generates RootName.cts)
False WrHAWCFF - [Envision addition] Output full-field time-series data in HAWC form? (Generates RootName-u.bin, RootName-v.bin, RootName-w.bin, RootName.hawc)
False WrFMTTF - Output full-field time-series data in formatted (readable) form? (Generates RootName.u, RootName.v, RootName.w)
False WRACT - Output coherent turbulence time steps in Aerodyn form? (Generates RootName.cts)
False ScaleIEC - Scale IEC turbulence models to exact target standard deviation? [=no additional scaling; 1=use hub scale uniformly; 2=use individual scales]

-----Turbine/Model Specifications-----
5 NumGrid_Z - Vertical grid-point matrix dimension
5 NumGrid_Y - Horizontal grid-point matrix dimension
0.01 TimeStep - Time step [seconds]
600 AnalysisTime - Length of analysis time series [seconds] (program will add time if necessary: AnalysisTime = MAX(AnalysisTime, UsableTime+GridWidth/MeanHHWS) )
"ALL" UsableTime - Usable length of output time series [seconds] (program will add GridWidth/MeanHHWS seconds unless UsableTime is "ALL")
90 HubHt - Hub height [m] (should be > 0.5*GridHeight)
162.00 GridHeight - Grid height [m]
162.00 GridWidth - Grid width [m] (should be >= 2*(RotorRadius+ShaftLength))
0 VFlowAng - Vertical mean flow (uplift) angle [degrees]
0 HFlowAng - Horizontal mean flow (skew) angle [degrees]

-----Meteorological Boundary Conditions-----
"IECKM" TurbModel - Turbulence model ("IECKAI", "IECKVN", "GP_LLJ", "NWTCP", "SMOOTH", "WF_UPW", "WF_ODT", "WF_14D", "TIDAL", "API", "USRINP", "USRVKM", "TIMESR", or "NONE")
"TurbSim_User.spectra", "TurbSim_User.timeSeriesInput" UserFile - Name of the file that contains inputs for user-defined spectra or time series inputs (used only for "USRINP" and "TIMESR" models)
"1-ed3" IECstandard - Number of IEC 61400-x standard (x=1,2, or 3 with optional 61400-1 edition number (i.e. "1-ED2") )
"B" IECTurbc - IEC turbulence characteristic ("A", "B", "C" or the turbulence intensity in percent) ("KHTEST" option with NWTCP model, not used for other models)
"NTM" IEC_WindType - IEC turbulence type ("NTM"=normal, "xETM"=extreme turbulence, "xEW1"=extreme 1-year wind, "xEWM50"=extreme 50-year wind, where x=wind turbine class 1, 2, or 3)
"default" ETMc - IEC Extreme Turbulence Model "c" parameter [m/s]
"default" WindProfileType - Velocity profile type ("LOG", "PL"=power law, "JET", "H2L"=Log law for TIDAL model, "API", "USR", "TS", "IEC"=PL on rotor disk, LOG elsewhere; or "default")
"TurbSim_User.profiles" ProfileFile - Name of the file that contains input profiles for WindProfileType="USR" and/or TurbModel="USRVKM" [-]
90 RefHt - Height of the reference velocity (URef) [m]
20 URef - Mean (total) velocity at the reference height [m/s] (or "default" for JET velocity profile) [must be 1-hr mean for API model; otherwise is the mean over AnalysisTime]
350 ZJetMax - Jet height [m] (used only for JET velocity profile, valid 70-490 m)
"default" PLExp - Power law exponent [-] (or "default")
"default" ZO - Surface roughness length [m] (or "default")

-----Non-IEC Meteorological Boundary Conditions-----
"default" Latitude - Site latitude [degrees] (or "default")
0.05 RICH_N0 - Gradient Richardson number [-]
"default" USStar - Friction or shear velocity [m/s] (or "default")
```

```

"default"   ZI          - Mixing layer depth [m] (or "default")
"default"   PC_UW      - Hub mean u'w' Reynolds stress [m^2/s^2] (or "default" or "none")
"default"   PC_UV      - Hub mean u'v' Reynolds stress [m^2/s^2] (or "default" or "none")
"default"   PC_VW      - Hub mean v'w' Reynolds stress [m^2/s^2] (or "default" or "none")

-----Spatial Coherence Parameters-----
"default"   SCMod1     - u-component coherence model ("GENERAL", "IEC", "NONE", or "default")
"default"   SCMod2     - v-component coherence model ("GENERAL", "IEC", "NONE", or "default")
"default"   SCMod3     - w-component coherence model ("GENERAL", "IEC", "NONE", or "default")
"default"   InCDec1    - u-component coherence parameters for general or IEC models [-, m^-1] (e.g. "10.0 0.3e-3" in quotes) (or "default")
"default"   InCDec2    - v-component coherence parameters for general or IEC models [-, m^-1] (e.g. "10.0 0.3e-3" in quotes) (or "default")
"default"   InCDec3    - w-component coherence parameters for general or IEC models [-, m^-1] (e.g. "10.0 0.3e-3" in quotes) (or "default")
"default"   CohExp     - Coherence exponent for general model [-] (or "default")

-----Coherent Turbulence Scaling Parameters----- [used only when WACT=TRUE]
".EventData"  CTEventPath - Name of the path where event data files are located
".random"     CTEventFile  - Type of event files ("LES", "DNS", or "RANDOM")
true          Randomize   - Randomizes the disturbance scale and locations? (true/false)
1             DistScl     - Disturbance scale [-] (ratio of event dataset height to rotor disk). (Ignored when Randomize = true.)
0.5           CTLy       - Fractional location of tower centerline from right [-] (looking downwind to left side of the dataset. (Ignored when Randomize = true.)
0.5           CTLz       - Fractional location of hub height from the bottom of the dataset. [-] (Ignored when Randomize = true.)
30            CTStartTime - Minimum start time for coherent structures in RootName.cts [seconds]

! NOTE: Do not add or remove any lines in this file!

```

References

- [1] Y. Liu and M. Chertkov, “Anomalous Response of Floating Offshore Wind Turbine to Wind and Waves,” Feb. 2024. [Online]. Available: <https://wes.copernicus.org/preprints/wes-2024-14/>
- [2] American Clean Power Association, “Wind power facts,” 2023, accessed: 2023-07-26. [Online]. Available: <https://cleanpower.org/facts/wind-power/>
- [3] G. Betti, M. Farina, G. A. Guagliardi, A. Marzorati, and R. Scattolini, “Development of a Control-Oriented Model of Floating Wind Turbines,” *IEEE Transactions on Control Systems Technology*, vol. 22, no. 1, pp. 69–82, Jan. 2014. [Online]. Available: <http://ieeexplore.ieee.org/document/6451223/>
- [4] J. Jonkman, S. Butterfield, W. Musial, and G. Scott, “Definition of a 5-mw reference wind turbine for offshore system development,” 2 2009. [Online]. Available: <https://www.osti.gov/biblio/947422>
- [5] D. Matha, “Model development and loads analysis of an offshore wind turbine on a tension leg platform with a comparison to other floating turbine concepts: April 2009,” 2 2010. [Online]. Available: <https://www.osti.gov/biblio/973961>
- [6] M. Karimi, M. Hall, B. Buckham, and C. Crawford, “A multi-objective design optimization approach for floating offshore wind turbine support structures,” *Journal of Ocean Engineering and Marine Energy*, vol. 3, pp. 1–19, 02 2017.
- [7] I. V. der Hoven, “Power spectrum of horizontal wind speed in the frequency range from 0.0007 to 900 cycles per hour,” *Journal of Atmospheric Sciences*, vol. 14, no. 2, pp. 160 – 164, 1957. [Online]. Available: https://journals.ametsoc.org/view/journals/atsc/14/2/1520-0469_1957_014_0160_psohws_2_0_co_2.xml
- [8] C. Nichita, D. Luca, B. Dakyo, and E. Ceanga, “Large band simulation of the wind speed for real time wind turbine simulators,” *IEEE Transactions on Energy Conversion*, vol. 17, no. 4, pp. 523–529, 2002.
- [9] G. Komen and K. Hasselmann, “On the existence of a fully developed wind-sea spectrum,” *Journal of Physical Oceanography - J PHYS OCEANOGR*, vol. 14, pp. 1271–1285, 08 1984.
- [10] A. B. Owen, “Change of Variables in Monte Carlo Integration.” [Online]. Available: <https://artowen.su.domains/mc/Ch-var-is.pdf>
- [11] B. B. Sorensen, A. Charalampopoulos, S. Zhang, B. Harrop, R. Leung, and T. Sapsis, “A non-intrusive machine learning framework for debiasing long-time coarse resolution climate simulations and quantifying rare events statistics,” Feb. 2024, arXiv:2402.18484 [physics]. [Online]. Available: <http://arxiv.org/abs/2402.18484>